PCCP

PAPER

View Article Online
View Journal | View Issue

Cite this: *Phys. Chem. Chem. Phys.*, 2024, **26**, 2440

Quality-dependent performance of hydrophobic ZIF-67 upon high-pressure water intrusion–extrusion process†

Eder Amayuelas, *[a] Luis Bartolomé, [a] Yan Zhang,[a] Juan Miguel López del Amo, [a] Oleksandr Bondarchuk,[b] Artem Nikulin,[a] Francisco Bonilla,[a] Elena Palomo del Barrio,[ac] Paweł Zajdel *[d] and Yaroslav Grosu *[ae]

Zeolitic imidazolate framework (ZIF) microporous materials have already been employed in many fields of energetic and environmental interest since the last decade. The commercial scale production of some of these materials makes them more accessible for their implementation in industrial processes; however, their massive synthesis may entail modifications to the preparation protocols, which may result in a loss in the optimization of this process and a drop in the material's quality. This fact may have implications for the performance of these materials during their lifetime, especially when they are used in applications such as energy dissipation, in which they are subjected to several operating cycles under high pressures. This study focuses on ZIF-67, a material that has demonstrated in the past its ability to dissipate energy through the water intrusion–extrusion process under high pressure. Two ZIF-67 samples were synthesized using different protocols, and 2 batches of different qualities (labelled as high quality (HQ) and low quality (LQ)) were obtained and analysed by water porosimetry to study their performance in the intrusion–extrusion process. Unexpectedly, minor structural differences, which are typically neglected especially under production conditions, had a dramatic effect on their performance. The results presented in this study reiterate the importance of quality control with respect to reproducibility of experimental results. In a broader perspective, they are critical to the technology transfer from academia to industry.

Received 24th July 2023,
Accepted 1st December 2023

DOI: 10.1039/d3cp03519k

rsc.li/pccp

1. Introduction

Crystalline microporous metal–organic frameworks known as MOFs are materials with increasing relevance in the field of energy and environmental remediation.[1,2] In particular, their sub-class – zeolitic imidazolate frameworks (ZIFs) established themselves in the last decade as interesting candidates for certain applications of industrial interest such as capture, storage and separation of gases,[3–6] luminescence,[7,8] magnetism,[9] heterogeneous catalysis,[10–12] and drug delivery.[13] ZIFs possess a 3D framework structure consisting of tetrahedrally coordinating divalent metal cations (as nodes) and bridging ditopic imidazolate (or benzimidazolate) anions (as ligands).[14,15] This arrangement gives rise to zeolite-like frameworks with several topologies but with larger pore size and volume. Moreover, some ZIFs displayed high thermal and chemical stability with a high hydrophobic character.[16,17] Therefore, ZIFs arise as references of microporous materials in many potential applications.[18–20]

In this regard, some of these materials are being produced on a large scale[21] facing industrial and environmental challenges due to their aforementioned capabilities. This fact paves the way for the generation of novel knowledge and the increasing number of studies regarding engineering, operation conditions and prototyping in emerging energetic fields.[18,22–24] In this context, some of these microporous materials have been studied previously by our group for energetic applications using intrusion–extrusion of water under high pressure.[25–30] By means of high-pressure intrusion of a non-wetting into a hydrophobic microporous material, mechanical energy could be converted into interfacial energy. Additionally, heat from the

[a] *Centre for Cooperative Research on Alternative Energies (CIC energiGUNE), Basque Research and Technology Alliance (BRTA), Alava Technology Park, Albert Einstein 48, 01510 Vitoria-Gasteiz, Spain. E-mail: eamayuelas@cicenergigune.com, ygrosu@cicenergigune.com*
[b] *International Iberian Nanotechnology Laboratory, Braga 4715-330, Portugal*
[c] *IKERBASQUE Basque Foundation for Science, Plaza Euskadi 5, 48009 Bilbao, Spain*
[d] *Institute of Physics, University of Silesia, 75 Pulku Piechoty 1, 41-500, Chorzów, Poland. E-mail: pawel.zajdel@us.edu.pl*
[e] *Institute of Chemistry, University of Silesia, Szkolna 9, 40-006 Katowice, Poland*

† Electronic supplementary information (ESI) available: Details on the characterization of all tested materials and Rietveld refinement details. See DOI: https://doi.org/10.1039/d3cp03519k

environment is harvested if the process is endothermic.[26,31,32] At least part of these energies can be converted into electricity *via* triboelectric effects.[33]

For this purpose, the structural features, topology and textural properties lead the way for the implementation of these materials in derived technological applications such as shock absorbers[34] or for nanotriboelectrification[35] where some nontrivial physical properties such as the crystal size or the macroscopic arrangement can have a great impact in their performances.[36,37]

The quality of the porous material, a concept already well-known by the materials science community but not accurately defined, is usually based on the materials' synthesis protocol, defects, level of purity and degradation process. With the increase in the production scale of the material, some properties that are not considered important for the desired application may be compromised. This in turn could play a crucial role in the performance of the material that may go unnoticed in the first test, but that comes out to light after several cycles of operation. To the best of our knowledge, the quality of ZIFs (and MOFs in general) has not been investigated for intrusion–extrusion applications.

In this work, we have tested two SOD-topology ZIF-67 batches of different qualities *via* water intrusion–extrusion experiments, confirming nonnegligible differences in their key performance characteristics. Deep characterization of the quality of the materials and their relationship with the synthesis led us to unravel the fundamental aspects of their performances and their impact on further technological applications.

2. Experimental

2.1. Materials

All solvents and chemicals were used as received from reliable commercial sources. Cobalt(II) nitrate hexahydrate 98% and methanol 96% were purchased from Fisher Scientific, 2-methylimidazole (HmIm) was purchased from Sigma-Aldrich Co. and ethanol (technical grade) was purchased from Scharlab S.L. ZIF-67 LQ was purchased from MOF Technologies.

2.2. ZIF-67 synthesis

Syntheses of ZIF-67 HQ and ZIF-L-Co samples were based on a previously reported study by H. Wu *et al.*,[38] with slight modification. For ZIF-67 HQ, two separate solutions of $Co(NO_3)_2{\cdot}6H_2O$ 80 mM and HmIm 320 mM were prepared in 100 mL of methanol. Both solutions were then mixed and stirred for one minute and the resulting mixture was left for crystallization at room temperature for 48 h. The supernatant was removed, and the purple precipitates were collected by centrifugation and washed thoroughly with ethanol three times. The final product was dried at 80 °C overnight. ZIF-67 LQ was ordered from MOF Technologies Company and was synthesized in a non-optimal Co : mIm ratio.

2.3. Characterization techniques

2.3.1. Infrared spectroscopy. The model of infrared spectrometer used for this work is Bruker Vertex 70. Infrared data were collected using the attenuated total reflectance (ATR) technique assembled in an argon-filled chamber. All the spectra were recorded for 128 scan times within the regime of 4000–400 cm^{-1}. The spectral resolution was 2 cm^{-1}.

2.3.2. Raman spectroscopy. Raman spectra were recorded with a Renishaw inVia confocal Raman spectrometer (serial number 16H981). An incident laser with a wavelength of 532 nm was focused using an inverted microscope (Leica) *via* a 50× objective lens (Leica). A 0.1% laser power and suitable filters were used to minimize the laser power and ensure not to create laser-induced damage to the micro-structure of the samples. All Raman spectra were collected in the range of 50–2000 cm^{-1}.

2.3.3. Nuclear magnetic resonance. ^1H solid state NMR experiments were performed using 200 MHz wide-bore (WB) solid state NMR spectrometers equipped with a 1.3 mm probe. Samples were spun at the magic angle at 50 kHz and the ^1H chemical shifts were referenced relative to bulk water resonating at 4.7 ppm. Single pulse experiments were conducted with a 90° pulse of 1.5 us and a recycle delay of 2s.

2.3.4. X-ray diffraction. The structural characterization was measured by means of X-ray diffraction at room temperature in powdered samples using a BRUKER-D8 ADVANCE X-ray diffractometer using CuKα (0.15406 nm) recorded in a 2θ step of 0.02° in the 5–80° range.

2.3.5. Nitrogen adsorption. The textural characterization was carried out using an automated gas adsorption analyzer (Micromeritics ASAP 2460). Nitrogen physisorption curves were recorded at −196 °C, after outgassing at 180 °C in a vacuum for 15 h. The specific surface area (S_{BET}) was calculated using the BET equation.[39,40] For the BET equation, we have used the linearization proposed by Parra *et al.*,[41] and the pore size distribution was obtained using the Barrett–Joyner–Halenda (BJH) model applied to the desorption isotherm branch. The total pore volume was calculated as the volume of gas adsorbed at a relative pressure of 0.99 in terms of $cm^3\ g^{-1}$, using the density of liquid gas to convert the amount of gas adsorbed under STP conditions with the expression $V_{(\text{TOTAL PORES})}$ ($cm^3\ g^{-1}$) = $V_{(\text{gas adsorbed})}$ ($cm^3\ g^{-1}$, STP) × 0.00154643.

2.3.6. Transmission electron microscopy (TEM). The TEM measurements were carried out using an FEI Tecnai F20 electron microscope operating at 200 kV. For TEM measurements, samples were placed without any solvent onto a holey carbon film fixed on a 3 mm copper grid.

2.3.7. PVT setup. The PV isotherms were measured using a high-pressure variable volume unit (HPVV-800) constructed by Eurotechnica. This unit consists of a piston drive module (XL NEMESYS) and a high-pressure syringe (10 mL) of steel, both from CETONI. The maximum pressure of the system is 80 MPa. The drive module is controlled by the software QmixElements which indicates and logs the pressure, the volume inside the syringe and the temperature in the unit. Moreover, the syringe body is directly connected to a cylindrical metallic vessel (∅ 20 mm and length 80 mm) where the samples are located to test. This metallic vessel (stainless steel 304L) and its connections were designed and self-own built at CIC energiGUNE. The pressure-transmitting fluid inside this vessel was

water. This PVT system can conduct tests in a temperature range of 278–523 K (5–250 °C). From 278 K to room temperature (RT), a self-built cryostat at CIC energiGUNE is placed around the vessel. This cryostat consists of a copper tube in a spiral to totally cover the length of the vessel with circulating water coming from a chiller bath (Julabo CORIO CD-1000F). The chiller circulator controls the temperature, and the PVT system logs the temperature using a thermocouple placed in the vessel. For temperatures higher than RT, a heating jacket built by Eurotechnica is adjusted in the vessel by increasing the temperature electrically. The temperature is controlled by a heating control which is connected to a thermocouple placed between the heating jacket and the vessel. ZIF-67 was encapsulated in a plastic cap which was wrapped with parafilm. This encapsulation was then placed into the PVT vessel where the sample is subjected to pressurization cycles.

2.3.8. X-ray photoelectron spectroscopy (XPS). The XPS measurements were performed using an XPS spectrometer (ESCALAB 250Xi, Thermo Scientific) equipped with a monochromatic Al-Kα X-ray radiation source (1486.6 eV) operated at a power of 200 W. The photoelectron spectra were collected at a take-off angle of 90° with respect to the sample surface by means of a hemispherical electron energy analyser operated in the constant analyser energy lens mode (CAE). The pass energies of 150 eV and 40 eV were used for the survey and high-resolution spectra, respectively. The binding energy was referenced by setting the binding energy of the C1s hydrocarbon peak (the most intensive component of the C1s spectrum) at 284.8 eV. An electron flood gun was used to compensate surface charging effects.

2.3.9. Thermogravimetric analysis. Thermogravimetric analysis was performed using a NETZSCH STA 449 F3 Jupiter thermal analyzer under a constant argon flow of 60 mL min^{-1} in the temperature range of 25–1000 °C with a heating rate of 10 °C min^{-1}.

2.3.10. Climatic chamber. The hydrophilicity of the samples was examined by combining exposure to 95% humidity using a Binder Model MKFT 115 climatic chamber, followed by thermogravimetric analysis. Around 30 mg of each sample was placed in a vial inside the climatic chamber at 30 °C at 95% humidity for 18 h. After this, the samples were kept in hermetically closed vials and then measured by thermogravimetric analysis up to 1000 °C as described in the previous section.

3. Results and discussion

Two ZIF-67 samples (ZIF-67 LQ and ZIF-67 HQ, where LQ and HQ stand for low quality and high quality, respectively) were characterized using different standard techniques, as described above, in order to deepen in the parameters that define their quality. The quality concept lies in the accordance of each XRD pattern with the theoretical model, *i.e.*, their similarity to the ideal structure (Fig. 1).

Differences in XRD patterns between different samples lie in the presence of a transient orthorhombic ZIF-L-Co phase formed in the early stages of the synthesis process (Fig. 1), as

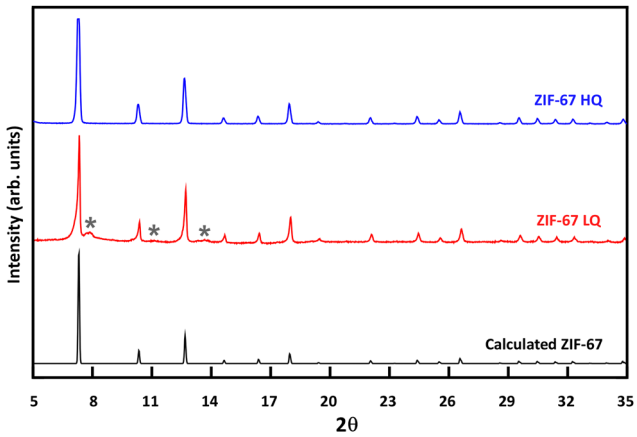

Fig. 1 XRD pattern of the synthesized ZIF-67 HQ and ZIF-67 LQ, compared to the theoretical model of ZIF-67 (* indicates ZIF-L-Co phase).

previously reported by J. Zhang *et al.*[42] The presence of this phase is related to the Co : mIm ratio used in the synthesis protocol, being minimized when applying the optimal ratio. A quantification of this transient phase through Rietveld refinement was tried with no success (Fig. S1–S4, ESI†) as the amount of these secondary peaks and their intensities are not enough for accurate identification. However, the appearance of a very broad reflection around 6.5 Å in *d*-spacing, which corresponds well with the layer thickness of the ZIF-L-Co phase, suggests that the extra phases are transition forms from the ordered-layered ZIF-L-Co to SOD. Such transition must rebuild the linkage of the structure, which would confirm the reported ZIF-L-Co transition to SOD ZIF-67.[42] Additionally, the structural reconstruction is reflected in a broadening of the reflections of the main ZIF-67 SOD phase. This ZIF-L-Co phase was also synthesized reducing drastically reaction time in order to confirm its presence during the synthesis process (Fig. S5, ESI†).

The extra peaks belonging to *hkl* planes related to the orthorhombic ZIF-L-Co transient phase increase in intensity with the decreasing quality of ZIF-67 which also has an impact on the crystal morphology as observed by TEM (Fig. 2a and b and Fig. S6, S7, ESI†): non-euhedral crystals and also non-regular crystal size distributions in the LQ sample. It is worth mentioning that the crystal size also varies between samples, a fact that has also an impact on the energy dissipation performance, as previously reported.[43] However, since the crystal size is above 100 nm for all the samples, according to Johnson *et al.*,[43] no significant impact of this parameter in their performances is found. Also, differences are shown in porosity as confirmed by the calculated micropore surface area and micropore volume (Fig. S8 and Table S1, ESI†).

The ZIF-67 HQ and ZIF-67 LQ samples were also characterized by means of infrared (Fig. S9 and Table S2, ESI†) and Raman spectroscopies (Fig. S10 and Table S3, ESI†). The FTIR spectra of both HQ and LQ samples are almost identical and characteristic vibration bands are in good agreement with previous literature studies,[44–48] as well as in the case of both Raman spectra.[48–52]

In addition, ^{1}H NMR experiments in the solid state were carried out for the synthesized samples (Fig. S11, ESI†). Two

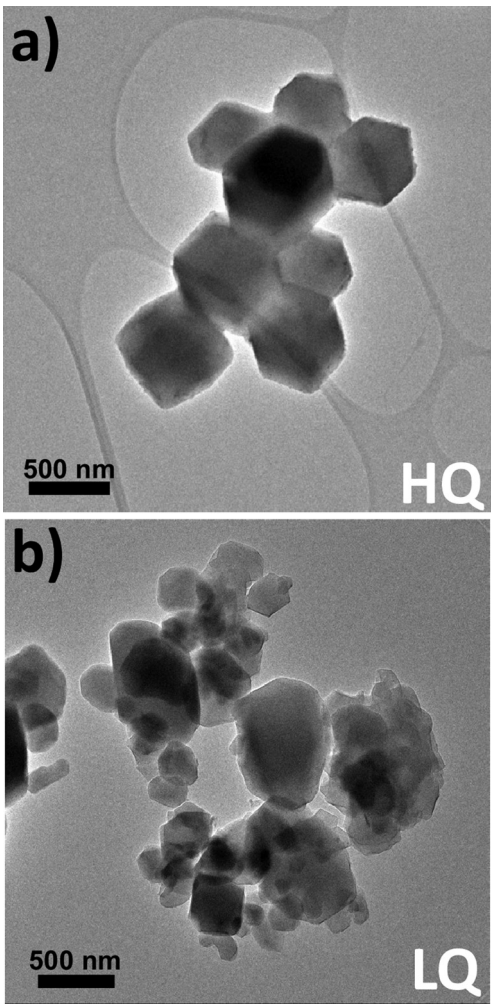

Fig. 2 TEM images of the dodecahedral ZIF-67 HQ and irregular ZIF-67 LQ.

main signals are observed for both samples at around 90 and 23 ppm. These signals are clearly out of the expected chemical shift range of ^{1}H NMR (typically from −2 to 15 ppm). This is in agreement with the presence of hyperfine shifts between the paramagnetic Co and the protons of the imidazole structures. Such paramagnetic shifts are commonly observed in compounds with transition metal sites and can be as large as several thousands of ppm in some cases.[53–55] The size and sign of a particular shift is a function of the bonds linking the metal to the nuclei under observation but a detailed analysis of this in our ZIF 67 samples is out of the scope of this work. The assignment of the signals is made considering the ratio of protons in each side as depicted in the figure. Additional signals are observed between 0 and 8 ppms that are clearly more intense in ZIF 67 LQ. These signals are in agreement with free imidazole molecules that are not shifted by interaction with the Co sites and are therefore out of the ZIF 67 structure. This is expected as ZIF-67 LQ was synthesized with an excess of the organic linker.

Finally, possible differences in the hydrophobicity of both samples were analyzed by thermogravimetric analysis after exposing both ZIF-67 HQ and ZIF-67 LQ to 95% of humidity in a climatic chamber. Fig. S12 in the ESI† shows that in the case of ZIF-67 LQ, there is 1–2% more mass loss compared to the HQ sample. Although it is a detectable difference, it is not very large since despite a very high level of humidity, under ambient pressure water adsorption would take place at the outer surface of crystallites. This outer surface is of course orders of magnitude lower compared to the inner hydrophobic surface of ZIF-67. Nevertheless, these results are in line with the hypothesis of a higher amount of defects in ZIF-67 LQ.

Thus, since the slight differences are purely structural between materials of different qualities, the similarity of the spectra of the previously described techniques is reasonable. This fact gives even more relevance to the fact that they go unnoticed when working with similar materials developed through non-identical synthesis protocols that may lead to the production of intermediate phases or impurities with undesirable characteristics, as in this case.

Fig. 3c and d show the topology of both structures: SOD-like cubic ZIF-67 which results in high porosity and surface area and robustness, and two-dimensional layered orthorhombic ZIF-L-Co. In this orthorhombic crystal structure, these layers constitute the building blocks for the further SOD topology,[56] in which the neighbouring two-dimensional SOD layers in ZIF-L-Co are not bridged by mIm, but by hydrogen bonds, giving rise to a non-porous structure with weaker structural areas between layers. As shown below, the concentration of the transient ZIF-L-Co phase in each tested sample can be used as a quantitative indicator of the quality of ZIF-67 and hence its performance under water intrusion–extrusion cycling.

Water intrusion–extrusion experiments were carried out using a high-pressure PVT-setup at room temperature up to 300 bar. According to PV-isotherms (Fig. 4a and b), water intrusion can be observed in both cases (HQ and LQ samples)

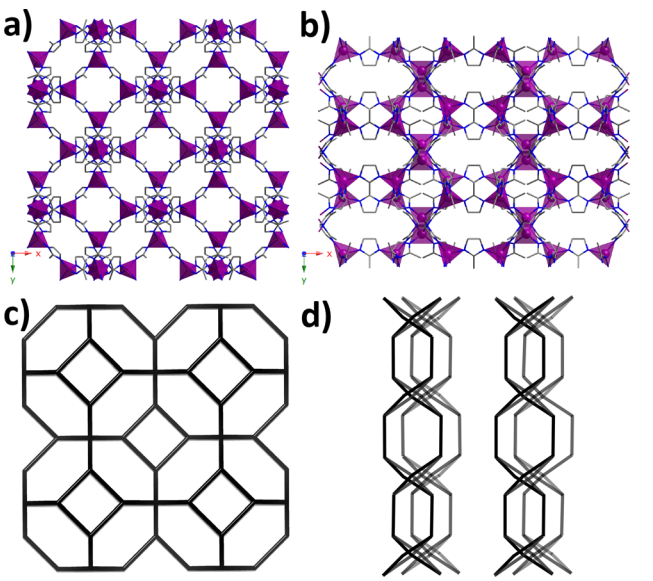

Fig. 3 Crystal structures of (a) porous cubic ZIF-67 and (b) non-porous orthorhombic ZIF-L-Co. (c) SOD-type topology of cubic ZIF-67. (d) Layered topology of orthorhombic ZIF-L-Co.

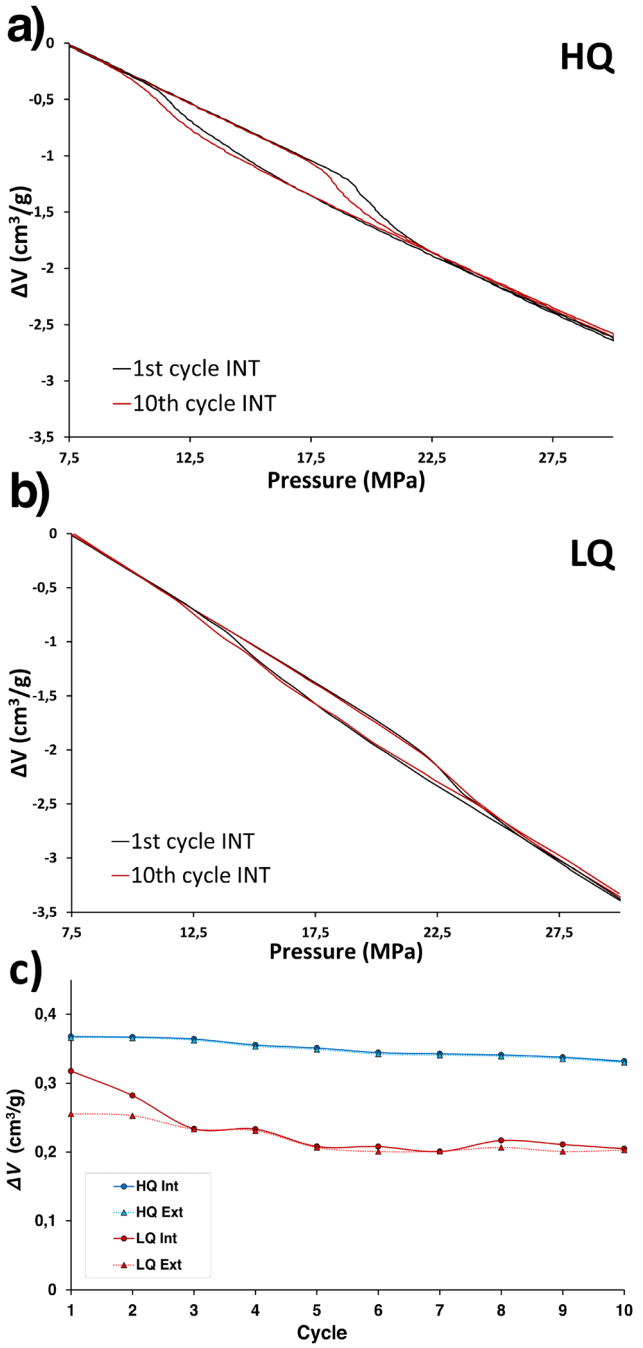

Fig. 4 PV isotherms of (a) ZIF-67 HQ and (b) ZIF-67 LQ. (c) Evolution of V_{int} and V_{ext} during successive cycles of ZIF-67 HQ and ZIF-67 LQ.

at relatively high pressures due to the hydrophobicity of ZIF-67. However, the characteristic values of the intrusion volume (V_{int}) drastically change depending on the material quality (Fig. 4c). While ZIF-67 HQ shows an intrusion volume of 0.36 $cm^3\ g^{-1}$, ZIF-67 LQ shows an intrusion volume of 0.31 $cm^3\ g^{-1}$. The same fact is shown for the extrusion volume (V_{ext}), since it is a higher value for ZIF-67 HQ (0.36 $cm^3\ g^{-1}$) and a much lower one for LQ (0.25 $cm^3\ g^{-1}$).

Considerable differences between the HQ and LQ samples in V_{int}/V_{ext} emerge as a result of small structural differences

Table 1 Intrusion/extrusion volume values for ZIF-67 HQ and ZIF-67 LQ in the 1st and 10th intrusion–extrusion cycles

	Intrusion/extrusion volume – 1st cycle V_{int}/V_{ext} ($cm^3\ g^{-1}$)	Intrusion/extrusion volume – 10th cycle V_{int}/V_{ext} ($cm^3\ g^{-1}$)
ZIF-67 HQ	0.36/0.36	0.33/0.33
ZIF-67 LQ	0.31/0.25	0.2/0.2

(defects, crystallinity, and disordered domains), highlighted by the higher concentration of the transient phase in the LQ phase, a consequence of its synthesis protocol. The structural features of the present ZIF-L-Co phase do not allow to host as many water molecules as a high-purity cubic ZIF-67 sample.

Most importantly, the quality of ZIF-67 samples has a drastic effect on their stability upon water intrusion–extrusion cycling. According to Fig. 4c, the V_{int}/V_{int} values are clearly more stable for the higher quality sample than those for the lowest quality one, being consistent with the basis explained above. ZIF-67 HQ, consisting of the highly pure cubic ZIF-67 porous and robust phase, exhibit a variation of V_{int}/V_{ext} from 0.35 to 0.32 $cm^3\ g^{-1}$ during successive cycles (Table 1). However, ZIF-67 LQ consisting of a mixture of cubic ZIF-67 with a higher proportion of ZIF-L-Co suffer a dramatic decrease of V_{int} in the second cycle from 0.31 $cm^3\ g^{-1}$ to 0.28 $cm^3\ g^{-1}$ and to 0.23 $cm^3\ g^{-1}$ in the third cycle when continues decreasing down to 0.2 $cm^3\ g^{-1}$ (Table 1 and Table S4, ESI†). The fundamental beneath this stability performance lies in the presence of the non-porous layered ZIF-L-Co related-phase with different proportions in each sample, which has an impact on the degradation process during the cycles. In other words, the concentration of the ZIF-L-Co phase not only indicates the loss of porosity (due to a lower amount of the cubic porous ZIF-67 phase available per gram of the sample), but also indicates that the available cubic porous ZIF-67 phase has lower stability, possibly due to the poorer ideality of the structure (lower crystallinity, higher concentration of defects, lower hydrophobicity affected by the latter, *etc.*). In this regard, in order to confirm if the secondary phase related to ZIF-L-Co not only indicates the quality of the structure, but also affects to the stability of the sample, we measured 10 H_2O intrusion–extrusion cycles using a 50 : 50 wt% physical mixture of pure ZIF-67 HQ and pure ZIF-L-Co (the high concentration of ZIF-L-Co was used with the purpose of enhancing the possible effect of this phase in the stability). Results presented in Fig. S13 in the ESI† show that the presence of ZIF-L-Co or its degradation products does not affect the stability of well-crystalized ZIF-67 (ZIF-67 HQ). This is in bright contrast to ZIF-67 LQ that loses about 30% of its intrusion volume during the first five cycles. This observation is in line with our original message that the presence of ZIF-L-Co can serve as an indicator of the quality of the ZIF-67 sample due to a non-optimized synthesis protocol.

Another difference between both materials is related to the intrusion pressure (P_{int}), since in the case of ZIF-67 LQ it is slightly higher. This could be caused by the presence of unreacted imidazoles (confirmed by ^1H NMR as previously mentioned), affecting the intrusion process *via* the surface properties of the liquid or partial pores blocking and, in the end, increasing the P_{int}.

The powdered ZIF-67 HQ and LQ samples were characterized by means of X-ray diffraction after intrusion–extrusion tests to confirm structural modifications and new possible degradation products during the water intrusion process and successive cycles. XRD patterns (Fig. S14 and S15, ESI†) evidence changes in both ZIF-67 samples, broadening the previously reported knowledge about the structural stability of ZIF-67 in water under pressure.[34]

One can observe an amorphization of the material, evident in the increment of background at lower 2θ positions in the LQ sample and slightly in the HQ sample (which could mean that amorphous and unidentified phases could result from the intrusion–extrusion process). Both tested samples show new peaks related to at least one identified degradation product, Co_3O_4, which is in good agreement with the literature.[38] A quantitative analysis of all phases present in tested samples was carried out *via* the Rietveld refinement allowing us to quantify the proportion of the cubic ZIF-67 phase and different degradation products (Fig. S16–S19, ESI†). Through this refinement process, we observed that the ZIF-L-Co phase is not present in the tested samples.

In addition, $Co(OH)_2$ was identified as one of the degradation products for LQ (which contains the ZIF-L-Co related phase before cycling), but not for HQ (does not contain the ZIF-L-Co related phase before cycling). This may suggest that $Co(OH)_2$ is the degradation product of the ZIF-L-Co phase. To confirm this, we performed water intrusion–extrusion cycling for specifically synthesized ZIF-L-Co under the same conditions as that for ZIF-67 HQ and LQ. Since the ZIF-L-Co phase is not porous, no observable water intrusion step was recorded. The quantification analysis *via* the Rietveld refinement (Fig. S20, ESI†) of ZIF-L-Co after 10 cycles shows the only degradation products to be $Co(OH)_2$.

To assess the surface modifications due to the intrusion–extrusion test HQ and LQ samples, XPS was deployed. Fig. S21 and S22 (ESI†) present the Co2p and O1s spectra before and after the tests. To infer the oxidation state from the Co2p spectrum, one needs to keep in mind that the positions of the $Co2p_{3/2}$ peak are virtually the same for Co2+ and Co3+ and the shape and positions of the satellite peaks must be taken into account. The Co2p spectra acquired for LQ and HQ samples before testing show a $Co2p_{3/2}$ peak at ~780–781 eV and a satellite peak at ~786 eV, which is the indicative of Co in the 2+ oxidation state. The shape of the Co2p spectrum in the HQ sample virtually remains the same upon the test. But the O1s spectrum reveals an additional peak at ~530 eV, the characteristic of metal oxide, so it can be assigned to CoO or/and $Co(OH)_2$ formation.[57] The O1s spectrum taken for the sample LQ after the test also shows an additional metal oxide peak and it is even more pronounced than that for the HQ sample. At the same time, the Co2p spectrum recorded for the LQ sample after the test reveals quite substantial differences in the satellite structure – peak at ~786 eV is not seen there anymore and the spectrum appears similar to what was reported for Co_3O_4,[57] which is in line with the above presented XRD results.

Finally, in order to confirm the presence of degradation products in cycled HQ and LQ samples, infrared spectroscopy measurements were carried out for the tested powders (Fig. S23 and Table S5, ESI†). Two characteristic bands are observed at 576 cm^{-1} and 663 cm^{-1} related to the Co–O stretching vibration in Co_3O_4,[58] in addition to other vibration bands at 558 cm^{-1} and 677 cm^{-1} belonging to Co(II)–O stretching and Co(III)–O stretching, respectively, related to the previously reported Co_3O_4 and $Co(OH)_2$ degradation products.[59] The higher intensity of these bands in the case of ZIF-67 LQ tested materials leads to think in the higher proportion of these degradation products in the low quality material, in agreement with previous XRD analysis. In this sense, the greater width of the band below 557 cm^{-1} in the spectrum of tested ZIF-67 LQ could be related to the presence of the ρ_w(CoOH) vibration,[58] overlapped in this case with the previous band, due to the low proportion of the $Co(OH)_2$ degradation product as determined by XRD quantification analysis.

4. Conclusions

As evidenced from the above, the differences in the preparation of ZIF-67 MOFs result in very different performances during high-pressure water intrusion–extrusion cycling. Two ZIF-67 batches were synthesized using different Co : mIm ratios and reaction times, resulting in two different qualities: high quality (HQ) and low quality (LQ). This assigned quality is inversely proportional to the presence of a transient phase, related to the known ZIF-L-Co. The presence of the non-porous ZIF-L-Co can serve as an indicator of the quality of ZIF-67. The differences between the as-synthesised HQ and LQ materials are barely detectable by means of common characterization techniques. This suggests that great caution should be taken in the production protocol of ZIF-67, and potentially of other ZIFs, especially for high-demanding applications such as intrusion–extrusion energy dissipation performance, column chromatography, *etc.* These results are important for scaling up MOF production while ensuring their quality and stability, particularly under humid and/or high-pressure hydrostatic conditions.

Conflicts of interest

The authors declare no competing financial interests.

Acknowledgements

This project leading to this application has received funding from the European Union's Horizon 2020 research and innovation programme under grant agreement No. 101017858. This work is also part of the grant RYC2021-032445-I funded by MICIN/AEI/10.13039/501100011033 and by the European Union NextGeneration EU/PRTR. This research received financial support based on Decision No. 2021/43/D/ST5/00062 from the National Science Center (Poland).

References

1 Q. Gao, J. Xu and X. H. Bu, Recent advances about metal–organic frameworks in the removal of pollutants from wastewater, *Coord. Chem. Rev.*, 2019, **378**, 17–31.

2 E. M. Dias and C. Petit, Towards the use of metal-organic frameworks for water reuse: A review of the recent advances in the field of organic pollutants removal and degradation and the next steps in the field, *J. Mater. Chem. A*, 2015, **3**(45), 22484, DOI: 10.1039/C5TA05440K.

3 T. H. Bae, E. D. Bloch, D. L. Rogow, J. A. Mason, Z. R. Herm and K. Sumida, *et al.*, Carbon Dioxide Capture in Metal–Organic Frameworks, *Chem. Rev.*, 2011, **112**(2), 724.

4 M. P. Suh, H. J. Park, T. K. Prasad and D. W. Lim, Hydrogen storage in metal-organic frameworks, *Chem. Rev.*, 2022, **112**(2), 782–835, DOI: 10.1021/cr200274s.

5 L. J. Murray, M. Dinc and J. R. Long, Hydrogen storage in metal–organic frameworks, *Chem. Soc. Rev.*, 2009, **38**(5), 1294. Available from: https://pubs.rsc.org/en/content/articlehtml/2009/cs/b802256a.

6 B. Chen, Z. Yang, Y. Zhu and Y. Xia, Zeolitic imidazolate framework materials: recent progress in synthesis and applications, *J. Mater. Chem. A*, 2014, **2**(40), 16811. Available from: https://pubs.rsc.org/en/content/articlehtml/2014/ta/c4ta02984d.

7 M. D. Allendorf, C. A. Bauer, R. K. Bhakta and R. J. T. Houk, Luminescent metal–organic frameworks, *Chem. Soc. Rev.*, 2009, **38**(5), 1330. Available from: https://pubs.rsc.org/en/content/articlehtml/2009/cs/b802352m.

8 Y. Cui, Y. Yue, G. Qian and B. Chen, Luminescent functional metal-organic frameworks, *Chem. Rev.*, 2012, **112**(2), 1126, DOI: 10.1021/cr200101d.

9 M. Kurmoo, Magnetic metal–organic frameworks, *Chem. Soc. Rev.*, 2009, **38**(5), 1353. Available from: https://pubs.rsc.org/en/content/articlehtml/2009/cs/b804757j.

10 J. Lee, O. K. Farha, J. Roberts, K. A. Scheidt, S. T. Nguyen and J. T. Hupp, Metal–organic framework materials as catalysts, *Chem. Soc. Rev.*, 2009, **38**(5), 1450. Available from: https://pubs.rsc.org/en/content/articlehtml/2009/cs/b807080f.

11 L. Ma, C. Abney and W. Lin, Enantioselective catalysis with homochiral metal–organic frameworks, *Chem. Soc. Rev.*, 2009, **38**(5), 1248. Available from: https://pubs.rsc.org/en/content/articlehtml/2009/cs/b807083k.

12 Y. Huang, Y. Zhang, X. Chen, D. Wu, Z. Yi and R. Cao, Bimetallic alloy nanocrystals encapsulated in ZIF-8 for synergistic catalysis of ethylene oxidative degradation, *Chem. Commun.*, 2014, **50**(70), 10115. Available from: https://pubs.rsc.org/en/content/articlehtml/2014/cc/c4cc04479g.

13 Y. Sun, L. Zheng, Y. Yang, X. Qian, T. Fu and X. Li, *et al.*, Metal–Organic Framework Nanocarriers for Drug Delivery in Biomedical Applications, *Nano-Micro Lett.*, 2020, **12**(1), 1–29. Available from: https://link.springer.com/article/10.1007/s40820-020-00423-3.

14 R. Banerjee, A. Phan, B. Wang, C. Knobler, H. Furukawa and M. O'Keeffe, *et al.*, High-throughput synthesis of zeolitic imidazolate frameworks and application to CO2 capture, *Science*, 1979, **319**(5865), 939, DOI: 10.1126/science.1152516.

15 A. Phan, C. J. Doonan, F. J. Uribe-Romo, C. B. Knobler, M. Okeeffe and O. M. Yaghi, Synthesis, structure, and carbon dioxide capture properties of zeolitic imidazolate frameworks, *Acc. Chem. Res.*, 2010, **43**(1), 58–67, DOI: 10.1021/ar900116g.

16 P. Küsgens, M. Rose, I. Senkovska, H. Fröde, A. Henschel and S. Siegle, *et al.*, Characterization of metal-organic frameworks by water adsorption, *Microporous Mesoporous Mater.*, 2009, **120**(3), 325.

17 K. S. Park, Z. Ni, A. P. Côté, J. Y. Choi, R. Huang and F. J. Uribe-Romo, *et al.*, Exceptional chemical and thermal stability of zeolitic imidazolate frameworks, *Proc. Natl. Acad. Sci. U. S. A.*, 2006, **103**(27), 10186. Available from: https://www.pnas.org.

18 Z. Lai, Development of ZIF-8 membranes: opportunities and challenges for commercial applications, *Curr. Opin. Chem. Eng.*, 2018, **20**, 78–85.

19 L. R. de Moura Ferraz, A. É. G. A. Tabosa, D. D. S. da Silva Nascimento, A. S. Ferreira, V. de Albuquerque Wanderley Sales, J. Y. R. Silva, S. Alves Júnior, L. A. Rolim, J. J. S. Pereira and P. J. Rolim-Neto, ZIF-8 as a promising drug delivery system for benznidazole: development, characterization, in vitro dialysis release and cytotoxicity, *Sci. Rep.*, 2020, **10**, 16815.

20 G. Lu and J. T. Hupp, Metal-organic frameworks as sensors: A ZIF-8 based fabry-pérot device as a selective sensor for chemical vapors and gases, *J. Am. Chem. Soc.*, 2010, **132**(23), 7832, DOI: 10.1021/ja101415b.

21 A. Deacon, L. Briquet, M. Malankowska, F. Massingberd-Mundy, S. Rudić and T. L. Hyde, *et al.*, Understanding the ZIF-L to ZIF-8 transformation from fundamentals to fully costed kilogram-scale production, *Commun. Chem.*, 2022, **5**(1), 1–10. Available from: https://www.nature.com/articles/s42004-021-00613-z.

22 C. Sun, J. H. Zhang, X. F. Yuan, J. N. Duan, S. W. Deng and J. M. Fan, *et al.*, ZIF-8-Based Quasi-Solid-State Electrolyte for Lithium Batteries, *ACS Appl. Mater. Interfaces*, 2019, **11**(50), 46671, DOI: 10.1021/acsami.9b13712.

23 P. D. Sutrisna, N. Prasetya, N. F. Himma and I. G. Wenten, A mini-review and recent outlooks on the synthesis and applications of zeolite imidazolate framework-8 (ZIF-8) membranes on polymeric substrate, *J. Chem. Technol. Biotechnol.*, 2020, **95**(11), 2767.

24 A. V. Sonawane and Z. V. P. Murthy, Synthesis and characterization of ZIF-8-based PVDF mixed matrix membranes and application to treat pulp and paper industry wastewater using a membrane bioreactor, *Environ. Sci.*, 2022, **8**(4), 881. Available from: https://pubs.rsc.org/en/content/articlehtml/2022/ew/d2ew00011c.

25 Y. Grosu, V. Eroshenko, J. M. Nedelec and J. P. E. Grolier, A new working mode for molecular springs: Water intrusion induced by cooling and associated isobaric heat capacity change of a {ZIF-8 + water} system, *Phys. Chem. Chem. Phys.*, 2015, **17**(3), 1572.

26 Y. Grosu, G. Renaudin, V. Eroshenko, J. M. Nedelec and J. P. E. Grolier, Synergetic effect of temperature and pressure on energetic and structural characteristics of {ZIF-8 + water} molecular spring, *Nanoscale*, 2015, **7**(19), 8803–8810.

27 Y. Grosu, S. Gomes, G. Renaudin, J. P. E. Grolier, V. Eroshenko and J. M. Nedelec, Stability of zeolitic imidazolate frameworks: effect of forced water intrusion and framework flexibility

dynamics, *RSC Adv.*, 2015, **5**(109), 89498. Available from: **https://pubs.rsc.org/en/content/articlehtml/2015/ra/c5ra19879h**.

28 V. Eroshenko, Y. Grosu, N. Tsyrin, V. Stoudenets, J. M. Nedelec and J. P. E. Grolier, Exceptionally large and controlled effect of negative thermal expansion in porous heterogeneous lyophobic systems, *J. Phys. Chem. C*, 2015, **119**, 19.

29 M. Tortora, P. Zajdel, A. R. Lowe, M. Chorążewski, J. B. Leão and G. V. Jensen, *et al.*, Giant Negative Compressibility by Liquid Intrusion into Superhydrophobic Flexible Nanoporous Frameworks, *Nano Lett.*, 2021, **21**(7), 2848, DOI: **10.1021/acs.nanolett.0c04941**.

30 G. Fraux, F. X. Coudert, A. Boutin and A. H. Fuchs, Forced intrusion of water and aqueous solutions in microporous materials: from fundamental thermodynamics to energy storage devices, *Chem. Soc. Rev.*, 2017, **46**(23), 7421. Available from: **https://pubs.rsc.org/en/content/articlehtml/2017/cs/c7cs00478h**.

31 T. Karbowiak, C. Paulin, A. Ballandras, G. Weber and J. P. Bellat, Thermal effects of water intrusion in hydrophobic nanoporous materials, *J. Am. Chem. Soc.*, 2009, **131**(29), 9898, DOI: **10.1021/ja903954h**.

32 A. R. Lowe, W. S. Y. Wong, N. Tsyrin, M. A. Chorążewski, A. Zaki and M. Geppert-Rybczyńska, *et al.*, The Effect of Surface Entropy on the Heat of Non-Wetting Liquid Intrusion into Nanopores, *Langmuir*, 2021, **37**(16), 4827–4835.

33 Y. Grosu, M. Mierzwa, V. A. Eroshenko, S. Pawlus, M. Chorazewski and J. M. Nedelec, *et al.*, Mechanical, Thermal, and Electrical Energy Storage in a Single Working Body: Electrification and Thermal Effects upon Pressure-Induced Water Intrusion-Extrusion in Nanoporous Solids, *ACS Appl. Mater. Interfaces*, 2017, **9**(8), 7044.

34 I. Khay, G. Chaplais, H. Nouali, G. Ortiz, C. Marichal and J. Patarin, Assessment of the energetic performances of various ZIFs with SOD or RHO topology using high pressure water intrusion–extrusion experiments, *Dalton Trans.*, 2016, **45**(10), 4392. Available from: **https://pubs.rsc.org/en/content/articlehtml/2016/dt/c5dt03486h**.

35 A. Lowe, N. Tsyrin, M. Chorażewski, M. L. J. B. Zajdel Pawe Land Mierzwa, M. Bleuel and T. Feng, *et al.*, Effect of Flexibility and Nanotriboelectrification on the Dynamic Reversibility of Water Intrusion into Nanopores: Pressure-Transmitting Fluid with Frequency-Dependent Dissipation Capability, *ACS Appl. Mater. Interfaces*, 2019, **11**, 40842, DOI: **10.1021/acsami.9b14031**.

36 I. Khay, G. Chaplais, H. Nouali, C. Marichal and J. Patarin, Water intrusion–extrusion experiments in ZIF-8: impacts of the shape and particle size on the energetic performances, *RSC Adv.*, 2015, **5**(40), 31514. Available from: **https://pubs.rsc.org/en/content/articlehtml/2015/ra/c5ra02636a**.

37 P. Zajdel, D. G. Madden, R. Babu, M. Tortora, D. Mirani and N. N. Tsyrin, *et al.*, Turning Molecular Springs into Nano-Shock Absorbers: The Effect of Macroscopic Morphology and Crystal Size on the Dynamic Hysteresis of Water Intrusion-Extrusion into-from Hydrophobic Nanopores, *ACS Appl. Mater. Interfaces*, 2022, **14**(23), 26699, DOI: **10.1021/acsami.2c04314**.

38 H. Wu, X. Qian, H. Zhu, S. Ma, G. Zhu and Y. Long, Controlled synthesis of highly stable zeolitic imidazolate framework-67 dodecahedra and their use towards the templated formation of a hollow Co3O4 catalyst for CO oxidation, *RSC Adv.*, 2022, **6**(9), 6915. Available from: **https://pubs.rsc.org/en/content/articlehtml/2016/ra/c5ra18557b**.

39 D. Dollimore, P. Spooner and A. Turner, The bet method of analysis of gas adsorption data and its relevance to the calculation of surface areas, *Surf. Technol.*, 1976, **4**(2), 121.

40 J. Rouquerol, F. Rouquerol, P. Llewellyn, G. Maurin and K. Sing, *Adsorption by Powders and Porous Solids*, 2nd edn, 2013, p. 646. Available from: **https://www.elsevier.com/books/adsorption-by-powders-and-porous-solids/rouquerol/978-0-08-097035-6**.

41 J. B. Parra, J. C. D. E. Sousa, R. C. Bansal, J. J. Pis and J. A. Pajares, Characterization of Activated Carbons by the BET Equation—An Alternative Approach, *Adsorpt. Sci. Technol.*, 2016, **12**(1), 51–66. Available from: **https://journals.sagepub.com/doi/10.1177/026361749501200106**.

42 J. Zhang, T. Zhang, D. Yu, K. Xiao and Y. Hong, Transition from ZIF-L-Co to ZIF-67: a new insight into the structural evolution of zeolitic imidazolate frameworks (ZIFs) in aqueous systems, *CrystEngComm*, 2015, **17**(43), 8212. Available from: **https://pubs.rsc.org/en/content/articlehtml/2015/ce/c5ce01531f**.

43 L. J. Johnson, G. Paulo, L. BartolomÕ, E. Amayuelas, A. Gubbiotti, D. Mirani, A. Le Donne, G. A. Lœpez, G. Grancini, P. Zajdel and S. Meloni, Optimization of the wetting-drying characteristics of hydrophobic metal organic frameworks *via* crystallite size: The role of hydrogen bonding between intruded and bulk liquid, *J. Colloid Interface Sci.*, 2023, **645**, 775–783, DOI: **10.1016/j.jcis.2023.04.059**.

44 M. Afkhami-Ardekani, M. R. Naimi-Jamal, S. Doaee and S. Rostamnia, Solvent-Free Mechanochemical Preparation of Metal–Organic Framework ZIF-67 Impregnated by Pt Nanoparticles for Water Purification, *Catalysts*, 2023, **13**(1), 9. Available from: **https://www.mdpi.com/2073-4344/13/1/9/htm**.

45 L. Zhang, A. Wu, M. Tian, Y. Xiao, X. Shi and H. Yan, *et al.*, 2-D porous Ni3N–Co3N hybrids derived from ZIF-67/Ni(OH)2 sheets as a magnetically separable catalyst for hydrogenation reactions, *Chem. Commun.*, 2018, **54**(79), 11088. Available from: **https://pubs.rsc.org/en/content/articlehtml/2018/cc/c8cc06099a**.

46 Y. Hu, X. Song, Q. Zheng, J. Wang and J. Pei, Zeolitic imidazolate framework-67 for shape stabilization and enhanced thermal stability of paraffin-based phase change materials, *RSC Adv.*, 2019, **9**(18), 9962. Available from: **https://pubs.rsc.org/en/content/articlehtml/2019/ra/c9ra00874h**.

47 L. Ma, X. Zhang, M. Ikram, M. Ullah, H. Wu and K. Shi, Controllable synthesis of an intercalated ZIF-67/EG structure for the detection of ultratrace Cd2 +, Cu2 +, Hg2+ and Pb2+ ions, *Chem. Eng. J.*, 2020, **395**, 125216.

48 A. Di Santo, H. Pérez, G. A. Echeverría, O. E. Piro, R. A. Iglesias and R. E. Carbonio, *et al.*, Exploring weak intermolecular interactions in thiocyanate-bonded Zn(II) and Cd(II) complexes with methylimidazole: crystal structures, Hirshfeld surface analysis and luminescence properties,

RSC Adv., 2018, **8**(42), 23891. Available from: **https://pubs.rsc.org/en/content/articlehtml/2018/ra/c8ra04452j**.

49 M. N. Jackson, M. K. Kamunde-Devonish, B. A. Hammann, L. A. Wills, L. B. Fullmer and S. E. Hayes, *et al.*, An overview of selected current approaches to the characterization of aqueous inorganic clusters, *Dalton Trans.*, 2015, **44**(39), 16982. Available from: **https://pubs.rsc.org/en/content/articlehtml/2015/dt/c5dt01268f**.

50 M. Wu, S. Chen, A. Soomro, S. Ma, M. Zhu and X. Hua, *et al.*, Investigation of synergistic effects and high performance of La-Co composite oxides for toluene catalytic oxidation at low temperature, *Environ. Sci. Pollu. Res.*, 2019, **26**(12), 12123, DOI: **10.1007/s11356-019-04672-7**.

51 G. Kumari, K. Jayaramulu, T. K. Maji and C. Narayana, Temperature induced structural transformations and gas adsorption in the zeolitic imidazolate framework ZIF-8: A Raman study, *J. Phys. Chem. A*, 2013, **117**(43), 11006, DOI: **10.1021/jp407792a**.

52 H. Yoon, A. Xu, G. E. Sterbinsky, D. A. Arena, Z. Wang and P. W. Stephens, *et al.*, In situ non-aqueous nucleation and growth of next generation rare-earth-free permanent magnets, *Phys. Chem. Chem. Phys.*, 2014, **17**(2), 1070. Available from: **https://pubs.rsc.org/en/content/articlehtml/2015/cp/c4cp04451g**.

53 D. S. Middlemiss, A. J. Ilott, R. J. Clément, F. C. Strobridge and C. P. Grey, Density functional theory-based bond pathway decompositions of hyperfine shifts: Equipping solid-state NMR to characterize atomic environments in paramagnetic materials, *Chem. Mater.*, 2013, **25**(9), 1723, DOI: **10.1021/cm400201t**.

54 J. Serrano-Sevillano, D. Carlier, A. Saracibar, J. M. Lopez Del Amo and M. Casas-Cabanas, DFT-Assisted Solid-State NMR Characterization of Defects in Li2MnO3, *Inorg. Chem.*, 2019, **58**(13), 8347, DOI: **10.1021/acs.inorgchem.9b00394**.

55 F. Dogan, J. R. Croy, M. Balasubramanian, M. D. Slater, H. Iddir and C. S. Johnson, *et al.*, Solid State NMR Studies of Li 2 MnO 3 and Li-Rich Cathode Materials: Proton Insertion, Local Structure, and Voltage Fade, *J. Electrochem. Soc.*, 2023, **162**(1), A235, DOI: **10.1149/2.1041501jes**.

56 Z. X. Low, J. Yao, Q. Liu, M. He, Z. Wang and A. K. Suresh, *et al.*, Crystal transformation in zeolitic-imidazolate framework, *Cryst. Growth Des.*, 2014, **14**(12), 6589, DOI: **10.1021/cg501502r**.

57 M. C. Biesinger, B. P. Payne, A. P. Grosvenor, L. W. M. Lau, A. R. Gerson and R. S. C. Smart, Resolving surface chemical states in XPS analysis of first row transition metals, oxides and hydroxides: Cr, Mn, Fe, Co and Ni, *Appl. Surf. Sci.*, 2011, **257**(7), 2717.

58 F. Zhang, C. Yuan, X. Lu, L. Zhang, Q. Che and X. Zhang, Facile growth of mesoporous Co3O4 nanowire arrays on Ni foam for high performance electrochemical capacitors, *J. Power Sources*, 2012, **203**, 250.

59 E. A. A. Aboelazm, G. A. M. Ali and K. Feng Chong, Cobalt Oxide Supercapacitor Electrode Recovered from Spent Lithium-Ion Battery, *Chem. Adv. Mater.*, 2018, **3**(4), 67–74.

